sciendo

CIVIL AND ENVIRONMENTAL ENGINEERING REPORTS

E-ISSN 2450-8594

CEER 2020; 30 (2): 0032-0054
DOI: 10.2478/ceer-2020-0018
Original Research Article

NUMERICAL SIMULATIONS OF DUCTILE FRACTURE IN STEEL ANGLE TENSION MEMBERS CONNECTED WITH BOLTS

Edyta BERNATOWSKA[1]
Rzeszów University of Technology, The Faculty of Civil and Environmental Engineering and Architecture, Poland

A b s t r a c t

The aim of the paper is to verify and present methodology for ultimate tensile resistance prediction in steel angle tension members connected to gusset plates with one row of bolts. After a description of the experimental investigations, the next step was to build numerical models. The subjects of the experiments consisted of single plate specimens with drilled holes and angles connected to gusset plates with 1, 2, 3, or 4 bolts. Close attention was given to choosing the appropriate material model, which takes into account the influence of microstructural damage and the process of ductile fracture initiation and propagation. The porous Gurson-Tvergaard-Needleman material model was analysed and the paper focuses on hierarchical validation of numerical models of steel angle bolted connections, which will then be used for parametric studies.

Keywords: steel angle, bolted connections, ultimate tensile resistance, finite element modelling, Gurson-Tvergaard-Needleman material model

1. INTRODUCTION

In civil engineering structures, steel angle members are commonly used as tension elements. For practical reasons, the most common form of joining such members is to connect them by a single leg with one or more bolts. Resistance of

[1]Corresponding author: Rzeszów University of Technology, The Faculty of Civil and Environmental Engineering and Architecture, Poznańska 2, 35-959 Rzeszów, Poland, e_bernat@prz.edu.pl, +48 (17)865-1629

tensile elements is based on such limiting states as plastic capacity of gross cross-section or ultimate tensile resistance of net cross-section, where the lower value decides resistance. In most cases, it is the second condition that determines the load capacity and is, therefore, involved with ductile fracture in critical cross-section. Bolted angles are an exceptional case because of existing eccentricities which affect the distribution of stresses in cross-section and hence their load capacity.

Contemporary design rules allow calculating of the ultimate tensile resistance of such elements as axially loaded, without time-consuming calculations of bending effects and stress concentrations but with some significant reduction of net cross-section. Despite the fact that many studies of such angles have been carried out [4, 27, 29, 32, 34, 35], there is relevant inconsistency between analytical models proposed in ruling codes (e.g. Polish Code [30], American [2] and Canadian Standards [3], or European Codes [9, 10]). Theoretical ultimate tensile resistance of the same angle computed according to these models achieves different values, which may lead to over- or underestimation of its load capacity.

To fully understand the behaviour of tensile angle connections and find out which of the proposed models define tensile resistance correctly, it is necessary to build an advanced numerical model of angle connection. Analysis of fracture, especially prediction of ductile fracture using micromechanics-based models, is, from a physical point of view, a completely different issue compared to well-known and established problems of plastic resistance. Hence, the numerical analysis requires careful definition of an appropriate material model, which takes into account the influence of microstructural damage on the load capacity and material strength.

This paper focuses on hierarchical validation of numerical models of steel angle tension members connected by one row of bolts, starting with a short description of experimental investigations. Afterwards, two types of material model (elastic-plastic and Gurson-Tvergaard-Needleman) are described and compared. The last stage is the development of a complete connection model.

2. EXPERIMENTAL INVESTIGATION

The experimental investigation consisted of three types of elements:

- standard tensile coupons which were used for determining the mechanical properties of steel,
- single tensile plates with drilled holes,
- angles connected with 1, 2, 3, and 4 bolts.

The standard tensile coupons were cut from the same plate as the elements with drilled holes, from angle-legs and gusset plates used in connections. They were prepared, tested, and their results were interpreted according to EN 10002-1 [7].

2.1. Single plates with drilled holes

Ten specimens were tested. The plates had the same cross-section dimensions and total length. They differed in hole diameter and its location. Seven specimens had one hole located symmetrically, two had double holes in the horizontal or vertical arrangement, and one had an eccentrically located hole. The geometry of the tested specimens is presented in Fig.1 and their description in Table 1. The specimens were divided into two groups as follows: plates with small holes (where the ratio d_0/b fell within the range from 0.17 to 0.34) and plates with large holes (where the ratio d_0/b fell within the range from 0.54 to 0.72). All the plates were made of steel with nominal grade S355. During experimental testing, all specimens were tensioned with displacement control until fracture of the net cross-section. An optical extensometer was used to measure the displacement of two marked points. Experimental tensile resistance N_{Ex} was assumed as the largest value of tensile force achieved during testing.

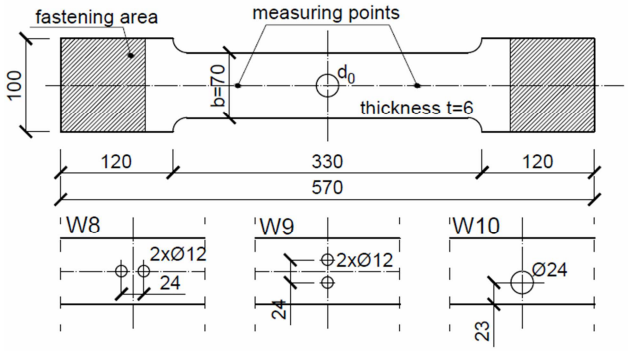

Fig. 1. Geometry of single plate specimens (dimensions in mm)

Table 1. Summary of single plate specimen results

Specimen	Nominal diameter [mm]	(d_0/b)	N_{EX} [kN]
W1	12	0.17	200.3
W2	18	0.26	182.0
W3	24	0.34	163.2
W4	30	0.43	141.3
W5	38	0.54	115.5
W6	42	0.59	101.9
W7	50	0.72	70.5
W8	2x12	0.17	202.7
W9	2x12	0.34	166.3
W10	24	0.34	148.9

2.2. Angles connected by a single leg with gusset plates

The next stage of experimental tests consisted of equal leg-angles connected to gusset plates with one row of bolts. 42 elements made of steel with nominal

grade S235 were tested. Three different sizes of angles were used (L50x5, L60x6, L80x6), varying in number (*n)* of bolts and longitudinal spacing (p_1) as well as edge distance of bolt holes perpendicular to force direction (e_2). All connections were designed so that the angle member was the weakest component of the joint and to cause its failure by net section fracture. For this purpose, fully threaded bolts M12 to M22 class 8.8 or 10.9 were used. Because the considered joints were category A according to EN 1993-1-8 [10], no preloading was required. However, to unify connection behaviour, a small clamping force F_p was applied during the assembly of all specimens. To induce failure on only one side of the member, bolt-hole clearance in the angles was differentiated. In the connection, at the point where the angle was supposed to rupture, bolt holes $d_{0,1}$ were drilled with appropriate clearance according to EN 1090-2 [6] regulations. In the second connection, bolt holes $d_{0,2}$ were equal to bolt nominal diameter (Fig. 2). The gusset plates used in the connection had the same cross-section, 10x100mm, and their total length depended on the number of bolts. Table 2 presents a description of six specimens chosen for a validation process.

Table 2. Summary of angle specimens chosen for a validation process

Specimen	**Cross-section**	**Bolt**	**n**	**e_1 [mm]**	**e_2 [mm]**	**p_1 [mm]**	**N_{Ex} [kN]**
J60/1/20/27	L60x6	M20 8.8	1	66	27	-	83.8
J80/1/22/36	L80x6	M22 8.8	1	75	36	-	149.3
J60/2/45/25	L60x6	M16 10.9	2	55	25	45	138.6
J60/3/45/25	L60x6	M16 10.9	3	55	25	45	180.7
J80/3/55/40	L80x6	M20 8.8	3	70	40	55	242.1
J80/4/55/40	L80x6	M20 8.8	4	70	40	55	268.6

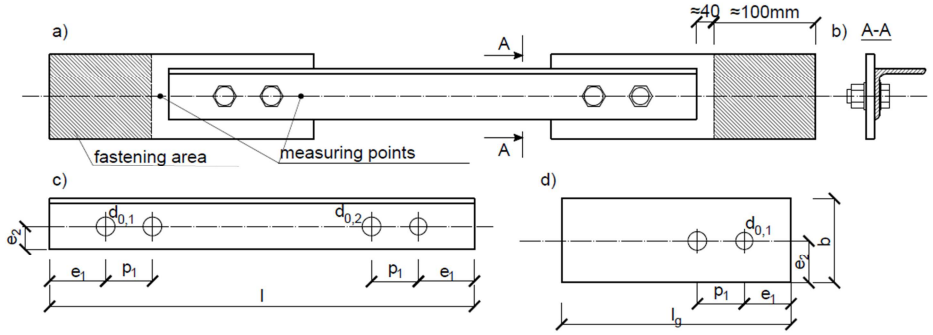

Fig. 2. Geometry of angle specimens

Similarly to single plates with holes, angle specimens were tensioned until fracture with displacement control and monitoring of force and displacement. In the connection with a single bolt, an optical extensometer was used, while in longer connections, inductive sensors G_i and D_i were implemented. In a small number of specimens, an electrofusion strain gauge was fixed at chosen points of the critical cross-section - *TD1/i*, and in some, at distance from it – *TD2/i*. Two inductive sensors B_i were used to monitor horizontal deflection in the middle of the angle length in two directions (Fig. 3).

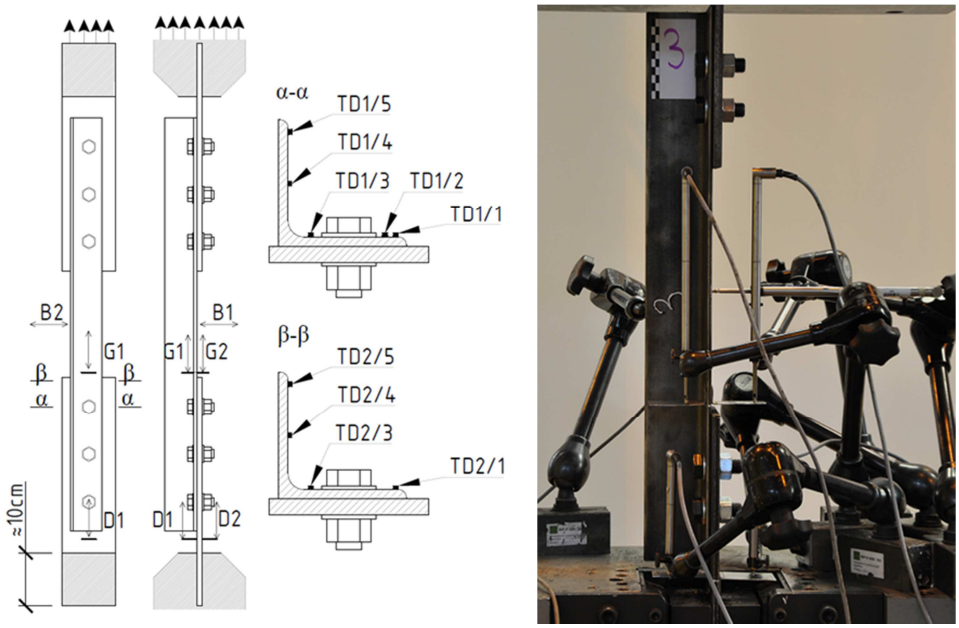

Fig. 3. Arrangement of sensors and strain gauges: a) scheme, b) real specimen

3. MATERIAL MODELS AND THEIR CHOICE

During the development of computational models built using the FE package ABAQUS [1], a choice between two types of material models was made. The considered materials were elastic-plastic (EP) and porous Gurson-Tvergaard-Needleman (GTN). The first of these included only elastic-plastic material characteristics. The second consisted of elastic-plastic characteristics and porous material model parameters. To verify their ability to predict the failure process in tensioned elements, results from single plates with drilled holes were also utilized. In order to create computer simulations of the elements and to calibrate the EP and GTN material models, results from standard tensile coupons were also used.

3.1 Elastic-plastic material model

Plastic material behaviour was represented by a multi-linear stress-strain curve in terms of true stress σ_{true} and true plastic strain $\varepsilon_{\text{true,pl}}$ calculated from the equations described below using nominal stress σ_{nom} and strain ε_{nom} values from experimental testing of standard tensile coupons:

$$\sigma_{truex} = \sigma_{nom}(1+\varepsilon_{nom}) \tag{3.1}$$

$$\varepsilon_{true,pl} = \ln(1+\varepsilon_{nom}) - \sigma_{true}/E \tag{3.2}$$

The elastic behaviour was defined by Young's modulus; E=210GPa and Poisson's ratio; v=0.3.

3.2 Porous material model

When considering the behaviour of elements working in non-linear ranges, far above the yield point, the use of classical methods of analysis based, e.g. on the Huber-Mises-Hencky (HMH) theory, is an inappropriate approach. It is necessary to implement material models based on fracture mechanics where the level of material damage is properly defined. In the case of metal materials, the process of initiation and fracture propagation is connected with microstructural damage occurring in the form of voids initiated on the non-metallic inclusions as well as precipitates present in the material. Generally, the mechanism of ductile fracture consists of several stages, as shown in figure 4. below.

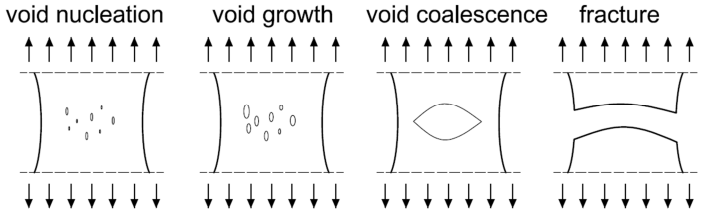

Fig. 4. Mechanism of ductile fracture (based on [22,23])

The destruction process takes place through the growth and coalescence of voids via localized plastic deformation. The material strength defined by normal stress σ is, therefore, closely related to its damage. The value of stress begins to decrease at the moment of microdamage initiation. Their growth causes the phenomenon of material softening, leading to its destruction at the moment of reaching a critical value.

The material model which takes into account the physical phenomena described above is the Gurson-Tvergaard-Needleman porous material model [13, 36, 37], which is recommended by Eurocode [11] and the scientific literature [33] as the

basic model for the assessment of failure conditions of building structures [15], i.e. also elements working in non-elastic ranges. The conducted research [14, 18-21,38,39] has shown that the use of the GTN model in the analysis of structural steel elements gives good convergence of the results obtained from numerical simulations and experimental tests. However, the aforementioned analyses did not consider the whole connection model.

Thanks to the implementation of GTN material in many engineering programs, it is possible to conduct analyses in the full range of structural work - from an unloaded state through to its ultimate destruction.

The yield condition in the GTN material model is expressed as follows:

$$\Phi = \left(\frac{\sigma_e}{\sigma_0}\right)^2 + 2q_1 f^* \cosh\left(q_2 \frac{3\sigma_m}{2\sigma_0}\right) - \left(1 + q_3 f^{*2}\right) = 0 \tag{3.3}$$

Where: Φ – non-dilatational strain energy, σ_e – effective stress according to the HMH hypothesis, σ_0 – yield stress of the material, σ_m - hydrostatic pressure (mean stress), f^*- modified void volume fraction, q_i – Tvergaard's parameters describing the plastic properties of the material.

The modified void volume fraction f^* is defined as follows:

$$f^* = \begin{cases} f & \text{for } f \le f_c, \\ f_c + \dfrac{\overline{f}_F - f_c}{f_F - f_c}(f - f_c) & \text{for } f_c < f < f_F, \\ \overline{f}_F & \text{for } f \ge f_F, \end{cases} \tag{3.4}$$

Where: f_c - critical void volume fraction at which the void coalescence starts, f_F - void volume fraction corresponding to the complete loss of the material strength, at final separation of the material.

When the material is not subjected to the loading and deformation, modified void volume fraction f^* is equal to the initial void volume fraction f_0, which is a basic GTN material parameter connected to the material porosity. The value of this parameter can be calculated based on the chemical composition (3.5) [14], where Mn and S are the values of manganese and sulphur inclusions determined from the code [8] or based on microstructural tests, counting the surface of non-metallic inclusions and precipitates of another phase related to the surface of the tested specimen.

$$f_0 = 0.054\left(S\% - \frac{0.001}{Mn\%}\right) \tag{3.5}$$

Critical void volume fraction f_c corresponds to the moment of the voids coalescence and occurs when the load capacity of the element decreases. It is related to the value f_0 [38], but it can also be determined by matching the σ-ε curve obtained from numerical simulations to that obtained from experimental tests, or by using microscopic photography [25]. The f_F value corresponds to the destruction of the material and for metals ranges from 0.10 to 0.20. It can also be determined from the relationship (3.6) or experimentally [24, 26].

$$f_F = 0.15 + 2f_0 \tag{3.6}$$

Parameters q_1, q_2, and q_3 from formula (3.3) are Tvergaard parameters defining some plastic properties of the material. For structural steels, typical values of these parameters are: q_1 = 1.5, q_2 = 1.0, and $q_3 = q_1^2$ = 2.25. However, the research described in [12] indicated the dependence of these parameters on Young's modulus E, yield stress σ_0, and the exponent of strengthening N.
The damage evolution is described by subsequent material parameters: f_N, ε_N, s_N. The first of them describes the volume fraction of nucleated voids (for structural steels this is assumed to be equal to 0.04 or determined during microstructural tests). The deformation level that creates new voids is described by the value ε_N. A typical value for steel is ε_N = 0.30. The normal distribution of voids nucleation strain is determined by the standard deviation s_N assumed to be in the range from 0.01 to 0.10. The relationship between these parameters is presented in equation (3.7).

$$\dot{f} = \dot{f}_{gr} + \dot{f}_{nucl} = (1-f)\dot{\varepsilon^{pl}}:\mathbf{I} + \frac{f_N}{s_N\sqrt{2\pi}}\exp\left[-\frac{1}{2}\left(\frac{\varepsilon_{em}^{pl}-\varepsilon_N}{s_N}\right)^2\right]\cdot\dot{\varepsilon_{em}^{pl}} \tag{3.7}$$

Where: $\dot{f}_{gr}$- change due to growth of voids existing in the material, $\dot{f}_{nucl}$ - change due to nucleation of new voids, $\dot{\varepsilon^{pl}}$ - plastic strain rate tensor, $\mathbf{I}$ - second-order unit tensor, ε_{em}^{pl} - equivalent plastic strain in the matrix material.
The influence of the described parameters on the force-displacement curve was presented in the example of a single plate specimen (W3) – Fig. 5.

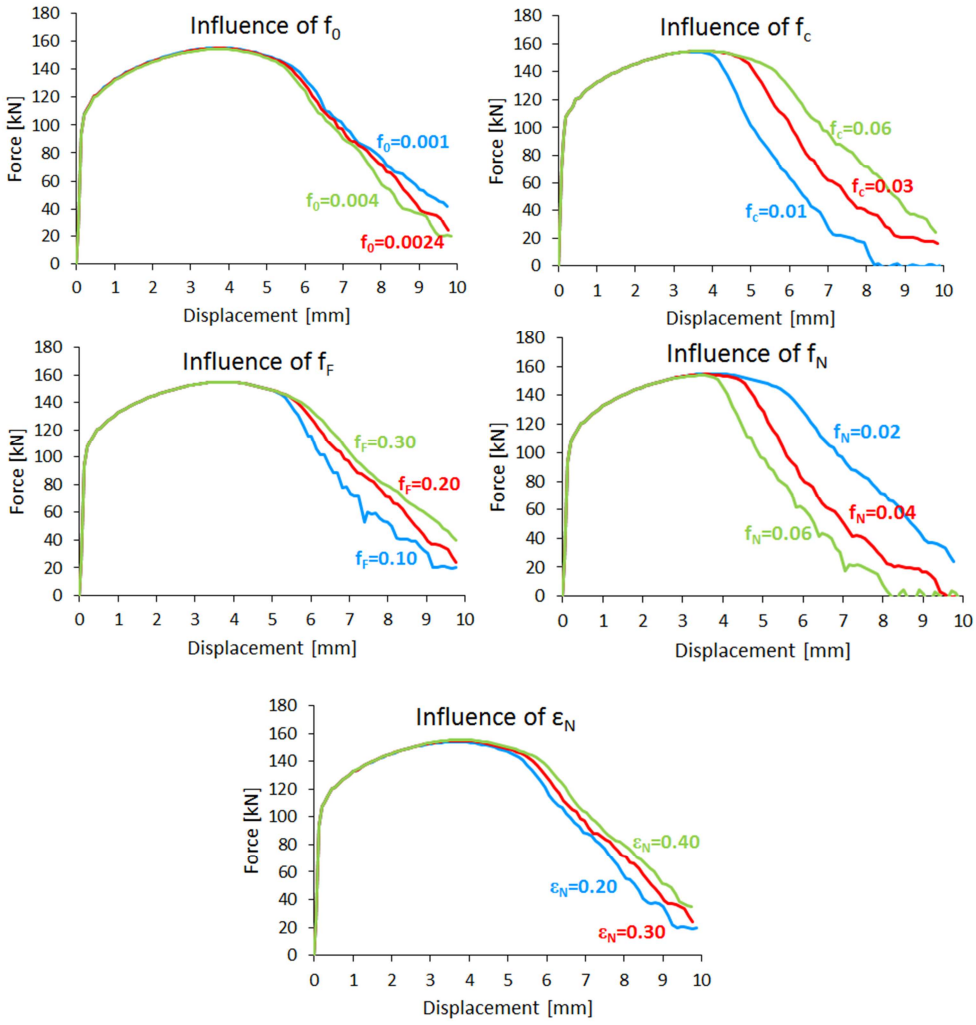

Fig. 5. Influence of GTN material parameters on the force-displacement curve in a single plate specimen

The final material parameters introduced to the ABAQUS [1] program are presented in Table 3.

Table 3. GTN material model parameters

Steel grade	f_o	q_i	f_N	ε_N	s_N	f_c	f_F
S355	0.0024	q_1=1.5 q_2=1.0 q_3=2.25	0.02	0.30	0.1	0.06	0.2
S235	0.001						

3.3 Choice of material model

The first stage of the validation process was a comparison between EP and GTN material models on standard tensile coupons cut from single plate specimens (S355), and from one angle size group (referential curves were used in this comparative study). The influence of material modelling is shown in Fig. 6. The compliance of the results is satisfactory for both types of material models; however, there is a difference in the slope of the curves after reaching the maximum tensile force when compared to FEA models with tests results.

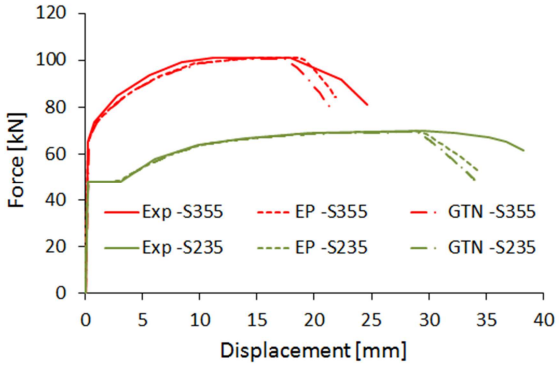

Fig. 6. Comparison of force-displacement curves for standard tensile coupons obtained from experimental tests and numerical simulations

The next stage was the implementation of EP and GTN to single plate models with drilled holes which are characterized by a larger degree of stress concentration compared to standard coupons. In this case, the obtained results are characterized by greater disjunction, as shown in Fig. 7 and 8.

In Table 4, the values of ultimate resistance corresponding to the maximum load level obtained in Finite Element analysis are shown. Values of N_{EP} correspond to ultimate resistance predicted by FE analysis with the EP material model and N_{GTN} is derived from the GTN material model. Values ΔN_{EP} and ΔN_{GTN} are the proportion of N_{EP}/N_{Ex} and N_{GTN}/N_{Ex}, respectively. The arithmetic mean of these values calculated for plates with small and large holes is described as $\overline{y}_{EP}$ and $\overline{y}_{GTN}$. It can be seen that both material models show the same degree of accuracy in their resistance domain. However, when comparing elongation, results obtained from numerical simulations demonstrate the influence of material modelling. As a reference to displacement capacity comparison, two points were taken into consideration:

- a point corresponding to ultimate resistance ($l_{Ex,ult}$, $l_{EP,ult}$ and $l_{GTN,ult}$ in Fig.7 and Table 5),

- a point on the descending part of each curve which corresponds to plastic resistance of the net cross-section of the specimen ($l_{Ex,y}$, $l_{EP,y}$ and $l_{GTN,y}$ in Fig.7 and Table 6).

Taking into account the results presented in Table 5 and Fig. 7 and 8, it can be said that both materials also show almost the same result when comparing elongation at maximum load level. Significant differences, however, appear in comparison of elongation corresponding to plastic resistance (Table 6).

The greatest accuracy in this displacement domain was observed in the case of the GTN material model and specimens with small holes. In real steel structures, a rather small proportion of d_0/b is used to keep the correct ratio between net section resistance and bolt resistance. Hence, GTN material is appropriate for angled bolted connections.

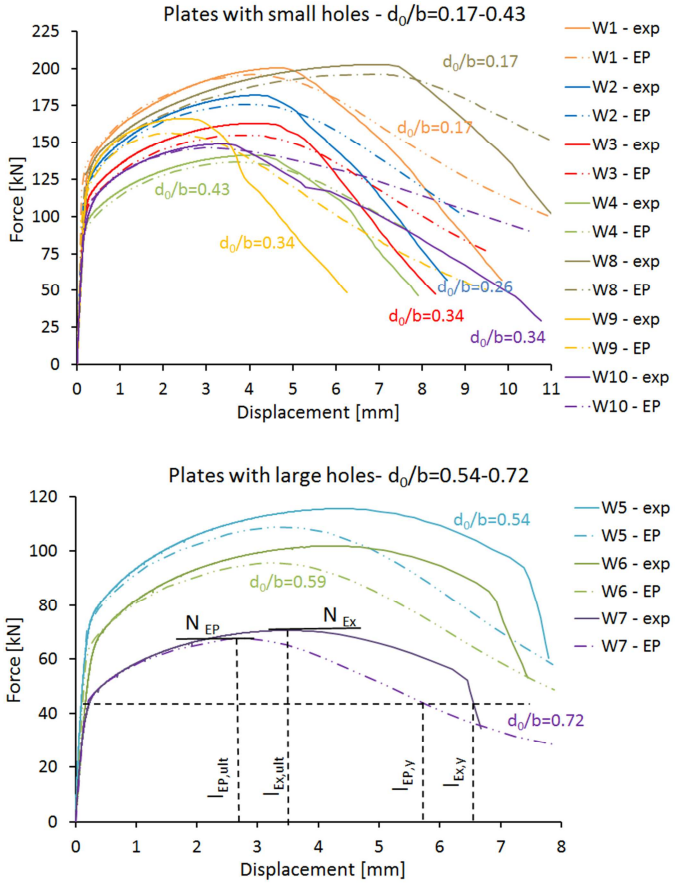

Fig. 7. Comparison of force-displacement curves for single plate specimens obtained from experimental tests and numerical simulations with the EP material model

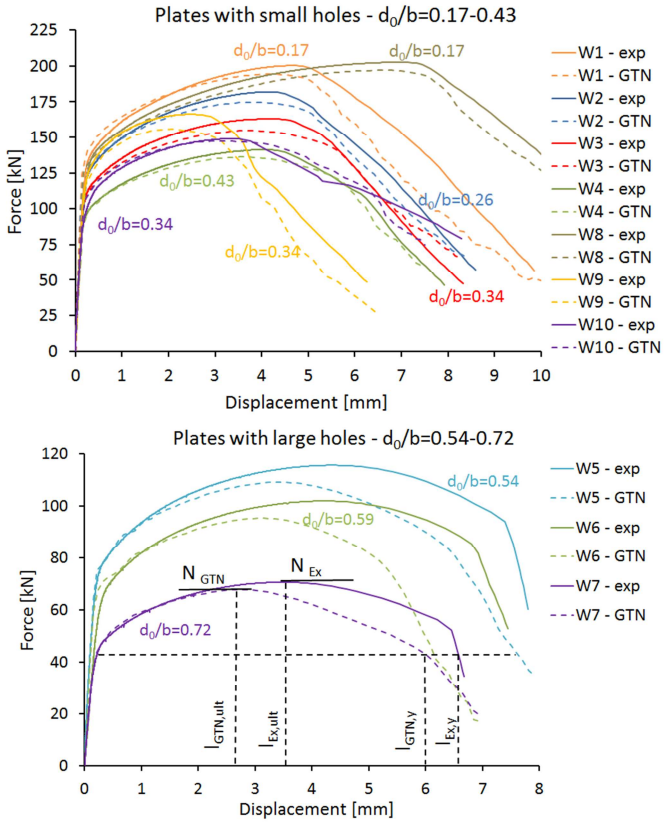

Fig. 8. Comparison of force-displacement curves for single plate specimens obtained from experimental tests and numerical simulations with the EP material model

Table 4. Comparison of maximum tensile force obtained from experimental tests and FEA models for single plate specimens

Symbol	**(d_0/b)**	**N_{EX} [kN]**	**N_{EP} [kN]**	**N_{GTN} [kN]**	**ΔN_{EP}**	**ΔN_{GTN}**	$\overline{y}_{EP}$	$\overline{y}_{GTN}$
W1	0.17	200.3	196.9	194.5	0.98	0.97		
W2	0.26	182.0	175.8	174.9	0.97	0.96		
W3	0.34	163.2	155.2	155.0	0.95	0.95		
W4	0.43	141.3	136.6	136.2	0.97	0.96	0.96	0.95
W8	0.17	202.7	196.2	197.0	0.94	0.94		
W9	0.34	166.3	156.3	155.9	0.94	0.93		
W10	0.34	148.9	146.2	147.3	0.96	0.96		
W5	0.54	115.5	108.9	109.0	0.97	0.97		
W6	0.59	101.9	95.6	95.2	0.94	0.96	0.96	0.97
W7	0.72	70.5	67.6	67.7	0.98	0.99		

Table 5. Comparison of elongation corresponding to ultimate resistance obtained from experimental tests and FEA models for single plate specimens

Symbol	**(d_0/b)**	**$l_{Ex,ult}$ [mm]**	**$l_{EP,ult}$ [mm]**	**$l_{GTN,ult}$ [mm]**	**$\Delta l_{EP,}$**	**$\Delta l_{GTN,}$**	$\overline{y}_{EP}$	$\overline{y}_{GTN}$
W1	0.17	4.6	4.1	4.1	0.89	0.89	0.92	0.91
W2	0.26	4.1	4.1	3.8	1.00	0.93		
W3	0.34	4.2	3.5	3.7	0.83	0.88		
W4	0.43	4.0	3.7	3.6	0.93	0.90		
W8	0.17	6.9	6.8	6.6	0.99	0.96		
W9	0.34	2.5	2.1	2.1	0.84	0.84		
W10	0.34	3.3	3.1	3.2	0.94	0.97		
W5	0.54	4.4	3.3	3.4	0.75	0.77	0.78	0.76
W6	0.59	4.2	3.3	3.1	0.79	0.74		
W7	0.72	3.5	2.8	2.7	0.80	0.77		

Table 6. Comparison of elongation corresponding to plastic resistance obtained from experimental tests and FEA models for single plate specimens

Symbol	**(d_0/b)**	**$l_{EX,y}$ [mm]**	**$l_{EP,y}$ [mm]**	**$l_{GTN,y}$ [mm]**	**$\Delta l_{EP,}$**	**$\Delta l_{GTN,}$**	$\overline{y}_{EP}$	$\overline{y}_{GTN}$
W1	0.17	7.7	9.4	6.7	1.22	0.87	1.22	0.94
W2	0.26	7.1	8.5	6.65	1.20	0.94		
W3	0.34	6.7	7.8	6.7	1.16	1.00		
W4	0.43	6.7	7.8	6.5	1.16	0.97		
W8	0.17	10.2	12.9	10.1	1.26	0.99		
W9	0.34	4.1	5.4	3.9	1.32	0.95		
W10	0.34	7.8	9.5	6.9	1.22	0.88		
W5	0.54	7.7	6.8	6.7	0.88	0.87	0.89	0.85
W6	0.59	7.2	6.7	5.6	0.93	0.78		
W7	0.72	6.6	5.75	6.0	0.87	0.91		

Looking at the following illustration (Fig. 9) it can be seen that the general behaviour of FEA models with GTN material is identical with real specimens. The sequence of initiation and propagation of fracture during experimental tests was the same as in the FE analyses. Hence, it can be said that the GTN material model gives good accuracy in both the resistance and displacement domain when modelling ductile fracture.

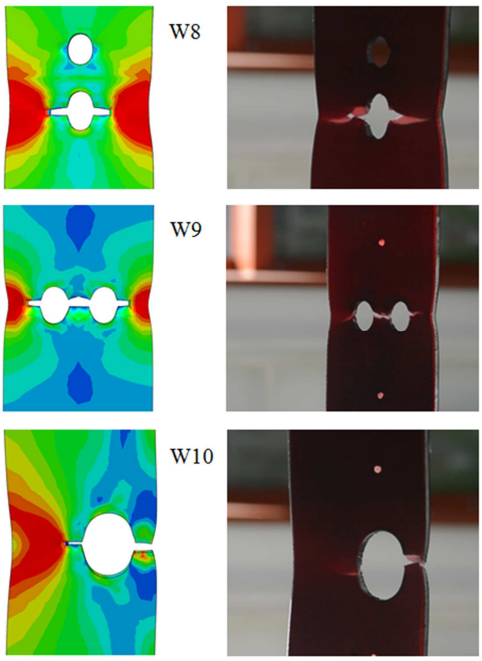

Fig. 9. Qualitative comparison of FEA models with GTN material, and experimental tests (specimens with drilled holes)

4. IMPLEMENTATION OF GTN MATERIAL MODEL TO ANGLE CONNECTION FE MODEL

After validation of the two material models on specimens with drilled holes, an angle connection model was built using the ABAQUS [1] package. For validation, the entire tested elements were modelled; however, subsequent analyses showed that the same results can be obtained when modelling half of the angle with the appropriate boundary conditions.

4.1 General description of joint FE model

The Finite Element model of the joint consisted of four components being the angle, the gusset plates, and bolts with nuts and washers (Fig. 10). Only the angle member, where fracture was expected, included the GTN material parameters. The remaining connection components had elastic-plastic characteristics (EP). Material properties of bolts were gained from bolts tensioning experiments. Implementation of the porous material model required carrying out Dynamic Explicit analysis. The influence of mesh density and bolt thread modelling (with or without thread) were also taken into account during the model building process. The implemented boundary conditions imitated the

real experiment: part of one gusset plate was fixed, the opposite part had blocked displacement in the *x* and *y* direction, while load in the *z*-direction in the form of displacement was applied.

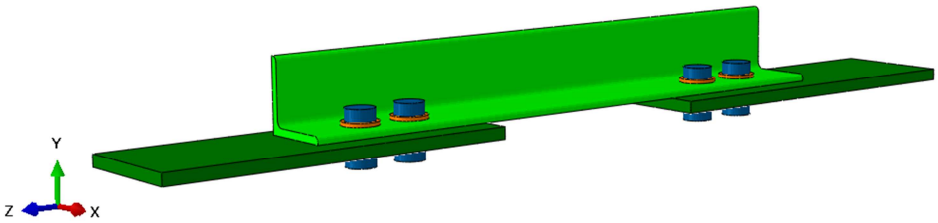

Fig. 10. Components of joint FE model (marked with different colours)

For the angle, gusset plates, and washers a C3D8R type of element was employed, defined as a three-dimensional, hexahedral 8-node linear brick with reduced integration. This type of element has proved to be suitable when simulating lap bolted connections [5, 17, 28, 31]. Bolts were built by using C3D8T and C3D6T elements, which are respectively 8-node thermally-coupled bricks with trilinear displacement and temperature, and a 6-node thermally-coupled triangular prism used to complete the mesh. To apply pre-tension force F_p over the bolts, a vertical thermal deformation method was utilised [16]. In this method, the thermal expansion coefficient is assumed to be unit and the temperature difference ΔT causing preload is calculated from equation (4.1). Contact between surfaces was defined using a general contact option. The frictional effects between surfaces were also included by incorporating the classical isotropic Coulomb friction model in the contact definition, with a friction coefficient μ equal to 0.1.

$$\Delta T = \frac{4F_p}{\pi d^2 E} \tag{4.1}$$

4.2 Results of numerical simulations of the bolted connection

To compare numerical simulations with experimental tests, force-displacement curves were used (Fig. 11-14) as well as the results from inductive sensors (Fig. 16) and an electrofusion strain gauge (Fig. 15). Table 7 presents the values of ultimate tensile resistance and corresponding elongation gained from experimental tests and FE analyses. These indicate good agreement of numerical simulations with the test results. The mean proportion of N_{GTN}/N_{Ex} is equal to 1.02 with standard deviation of 0.04. There is a slightly greater disjunction when it comes to elongation; the mean value of $l_{GTN,ult}/l_{Ex,ult}$ equals 0.85 with standard

deviation of 0.13. However, for some FE models, elongation corresponding to the maximum load level is almost the same as the experimental value. This disjunction may be a result of differences in elastic-plastic material characteristic (the referential strain-stress curves for each component were employed to FE model, while the individual standard coupons were characterized with different elongations).

Table 7. Comparison of experimental tests and FEA results for bolted connections

Specimen	$\mathbf{N_{Ex}}$ **[kN]**	$\mathbf{N_{GTN}}$ **[kN]**	$\mathbf{\Delta N_{GTN}}$	$\mathbf{l_{Ex,ult}}$ **[mm]**	$\mathbf{l_{GTN,ult}}$ **[mm]**	$\mathbf{\Delta l_{GTN}}$
J60/1/20/27	83.8	87.8	1.05	9.9	8.54	0.96
J80/1/22/36	149.3	140.6	0.94	20.6	13.0	0.63
J60/2/45/25	138.6	140.8	1.02	9.9	9.6	0.97
J60/3/45/25	180.7	184.4	1.02	11.4	10.4	0.91
J80/3/55/40	242.1	248.1	1.03	18.8	15.3	0.81
J80/4/55/40	268.6	283.8	1.06	17.7	14.8	0.84
		$\overline{y}_N$	1.02		$\overline{y}_l$	0.85

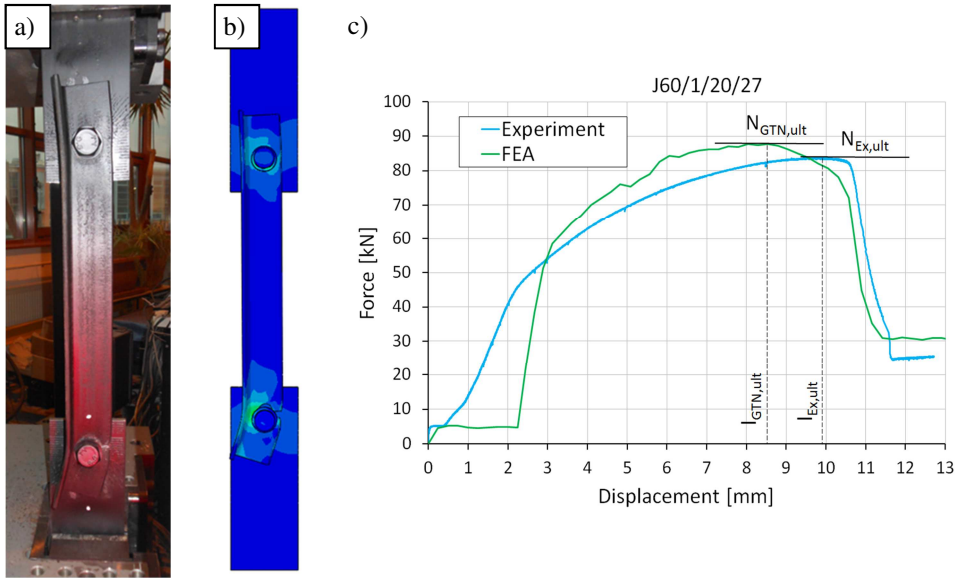

Fig. 11. Specimen J60/1/20/27: a) experimental test, b) FEA model, c) force-displacement curves gained from test and simulation

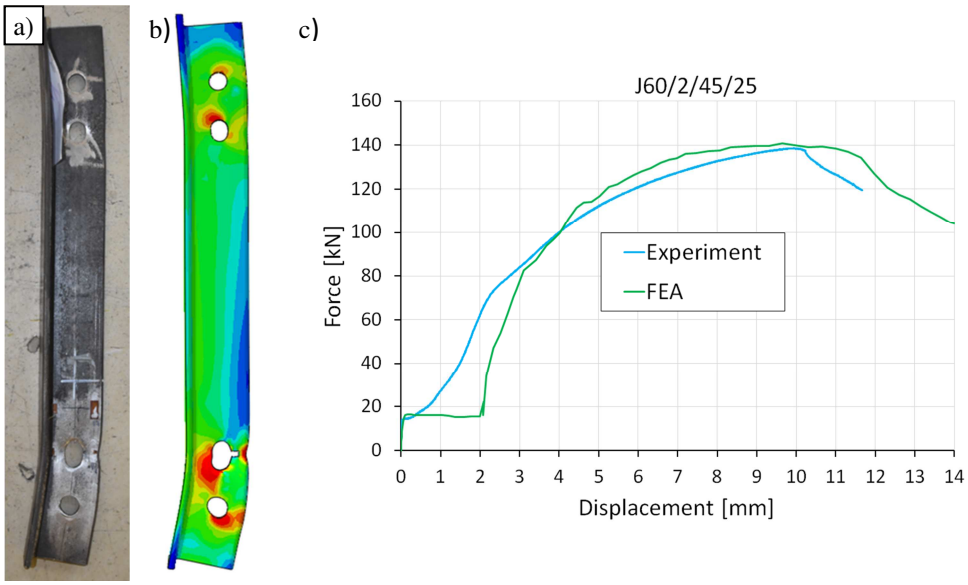

Fig. 12. Specimen J60/2/45/25: a) experimental test, b) FEA model, c) force-displacement curves gained from test and simulation

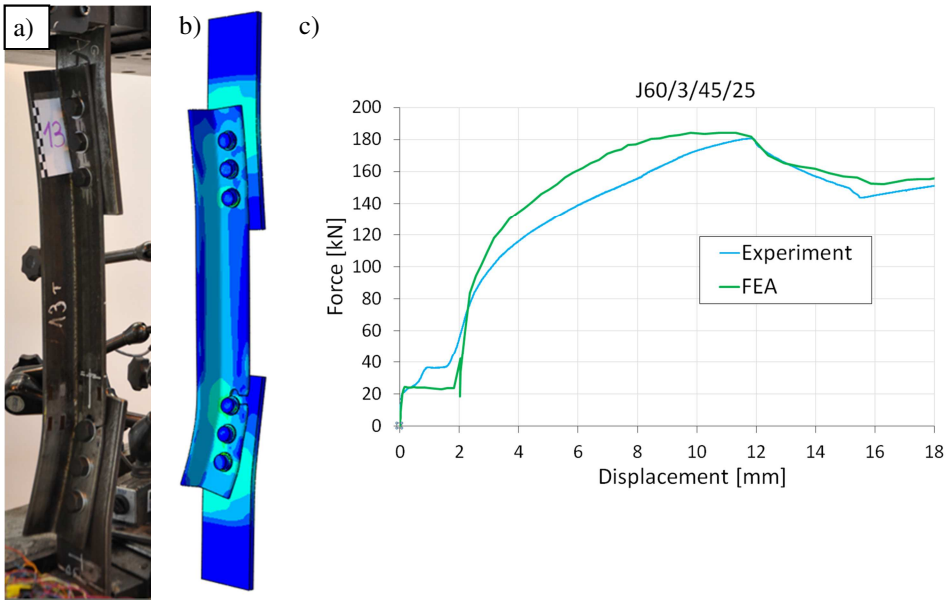

Fig. 13. Specimen J60/3/45/25: a) experimental test, b) FEA model, c) force-displacement curves gained from test and simulation

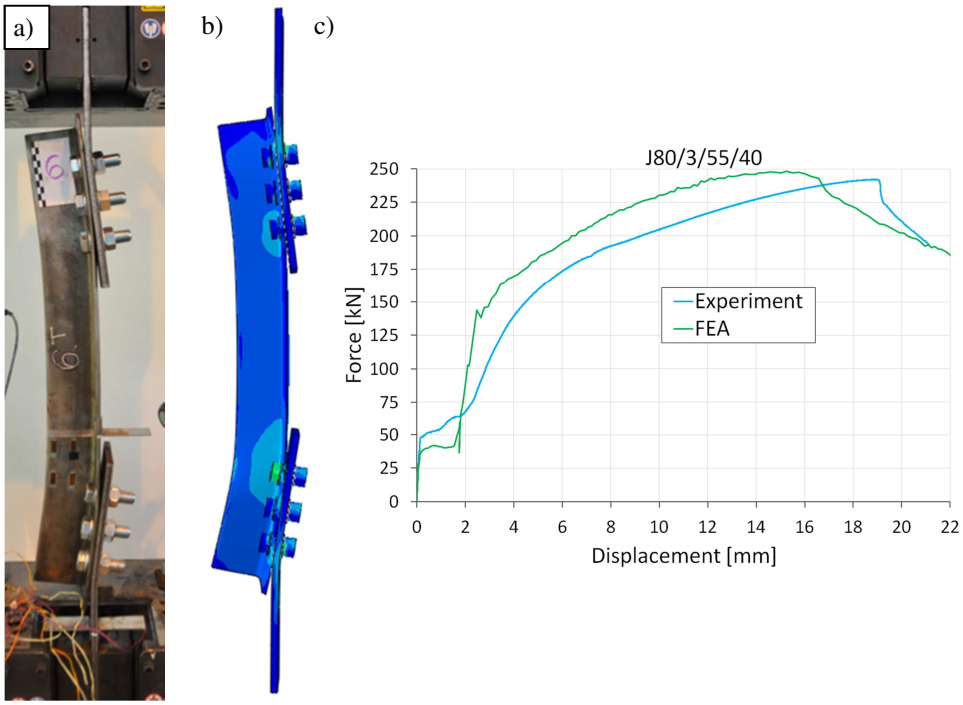

Fig. 14. Specimen J80/3/55/40: a) experimental test, b) FEA model, c) force-displacement curves gained from test and simulation

Values of real stress σ_{zz} at points corresponding to the electrofusion strain gauge arrangement (Fig. 3) were obtained from numerical models for various specific load levels (from $0.1N_{ult}$ to $1.0N_{ult}$). They were then compared with values of stresses calculated from the electrofusion strain gauge readings. An example comparison is shown in the illustration below (Fig. 15). Generally, all numerical models show a good degree of accuracy in the stress range σ_{zz} from zero to yield strength f_y. After reaching the yield point, the readings from the strain gauge can be improper and should not be taken into consideration.

Furthermore, horizontal deflections were measured in the FE models and compared with experimental tests results from inductive sensors B_1 and B_2 (Fig. 3). In this case, high compliance of results is also visible. Example curves of force vs. horizontal displacement are shown in Fig.16.

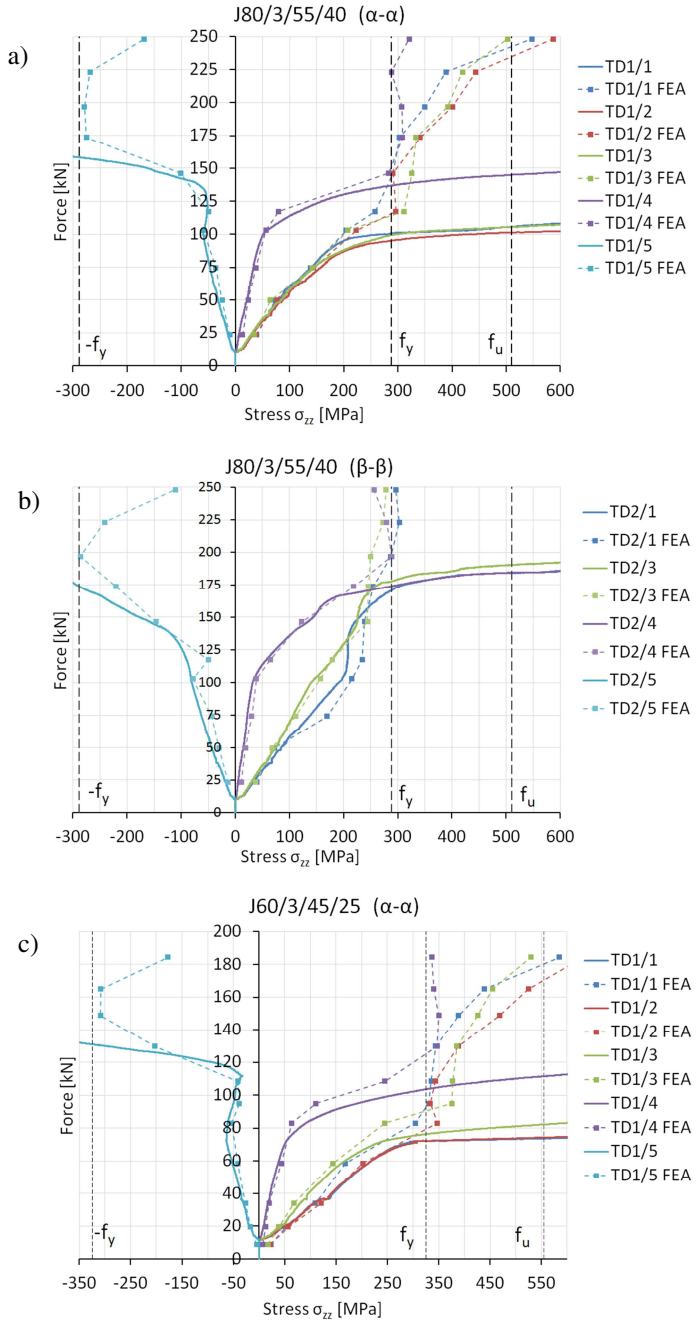

Fig. 15. Comparison of values of stresses σ_{zz} obtained from experimental tests and numerical simulations for a) and b) J80/3/55/40, c) J60/3/45/25 specimens

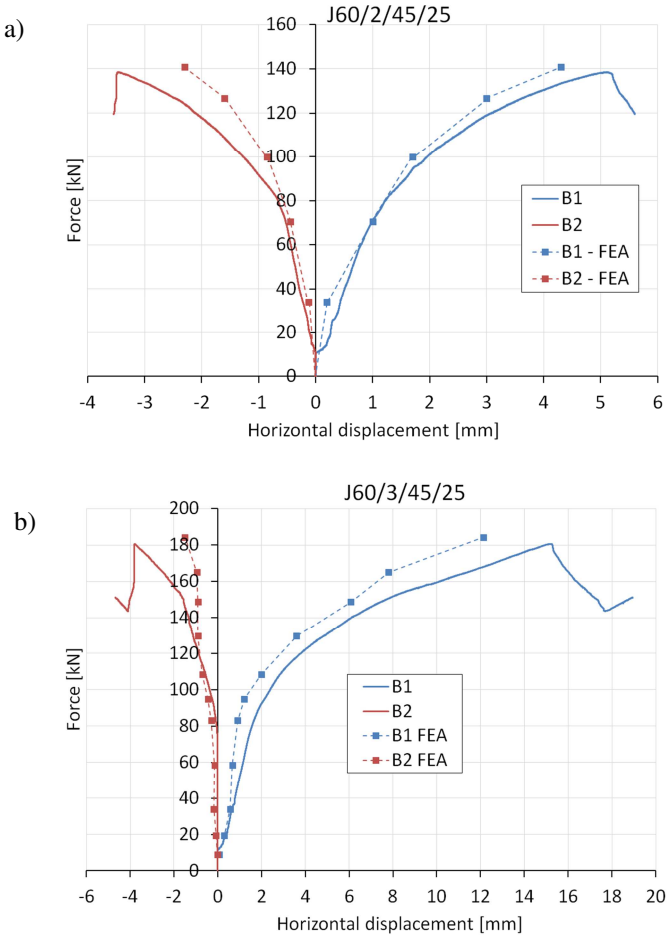

Fig. 16. Force-horizontal displacement curves gained from experimental tests and numerical simulations for a) J60/2/45/25 and b) J60/3/45/25 specimens

5. SUMMARY AND CONCLUSIONS

The paper presents a process of numerical model development which consists of steel angle-bolted connections under tension. Elements of hierarchical validation were used during the development of FEA models, built using the Abaqus program [1]. Two types of material model were presented being elastic-plastic and Gurson-Tvergaard-Needleman. The obtained results indicate good agreement between numerical simulation results and real experiments when GTN material was applied, both in the resistance and elongation domains. This allows further numerical simulations to be conducted on angles connected by bolts and to perform extensive parametric analyses for a large range of variables. It also makes it possible to conduct analyses in the full range of angle work,

from an unloaded state to its ultimate destruction. The final aim of the analyses will be verification of divergent analytical models for ultimate tensile resistance calculations, proposed in ruling codes [2, 3, 9, 10, 30] and the proposal of a new code, based on stress distribution in cross-section.

ADDITIONAL INFORMATION

This research was supported by a Polish Ministry of Science and Higher Education grant to maintain the research potential.

REFERENCES

1. Abaqus ver. 6.16
2. ANSI/AISC 360-10, Specification for Structural Steel Buildings 2010.
3. CAN/CSA S16-01 Limit state design of steel structure, Toronto, Canadian Standards Association, 2003.
4. Chesson, E and Munse, WH 1963. Riveted and bolted joints. *Journal of the Structural Division, ASCE* **89 (1)**, 67-126.
5. Draganić, H, Dokšanović, T and Markulak, D 2014. Investigation of bearing failure in steel single bolt lap connections. *Journal of Constructional Steel Research* **98**, 59–72.
6. EN 1090-2 Execution of steel structures and aluminium structures. Technical requirements for steel structures, 2011.
7. EN 10002-1 Metallic materials - Tensile testing – Part 1: Method of testing at ambient temperature, 2004.
8. EN 10025-1 Hot rolled products of structural steels - Part 1: General technical delivery conditions, 2007.
9. EN 50341-1 Overhead electrical lines exceeding AC 1 kV - Part 1: General requirements - Common specifications, 2013.
10. EN-1993-1-8: Eurocode 3: Design of steel structures - Part 1-8: Design of joints, 2005.
11. EN 1993-1-10: Eurocode 3: Design of steel structures - Part 1-10: Material toughness and through-thickness properties, 2005.
12. Faleskog, J, Gao X and Shih, CF 1998. Cell model for nonlinear fracture analysis – Micromechanics calibration. *International Journal of Fracture* **89**, **4**, 355-373.
13. Gurson, AL 1977. Continuum Theory of Ductile Rupture by Void Nucleation and Growth: Part I – Yield Criteria and Flow Rules for Porous Ductile Media. *Journal of Engineering Materials and Technology, Transactions of the ASME* **99, 1**, 2-15.
14. Hashemi, SH, Howard, IC, Yates, JR and Andrews, RM 2004. *Micro-mechanical damage modelling of notched bar testing of modern line pipe*

steel. The 15th European Conference of Fracture – Advanced Fracture Mechanics for Life and Safety, Stockholm, August, 11-26.
15. Kanvinde, A and Deierlein, G 2004. *Prediction of ductile fracture in steel moment connections during earthquakes using micromechanical fracture models*, 13th World Conference on Earthquake Engineering, Vancouver, B.C., Canada, August, 1-6, Paper No. 297.
16. Kim J, Yoon J and Kang, B 2007. Finite element analysis and modelling of structure with bolted joints. *Applied Mathematical Modelling* **31**, 895–911.
17. Kima, TS and Kuwamura, H 2007. Finite element modelling of bolted connections in thin-walled stainless steel plates under static shear. *Thin-Walled Structures* **45**, 407–421.
18. Kossakowski, P 2010. An analysis of the load-carrying capacity of elements subjected to complex stress states with a focus on microstructural failure. *Archives of Civil and Mechanical Engineering* **10, 2**, 15-39.
19. Kossakowski, P 2012. Zastosowanie mechaniki zniszczenia w analizie stanów awaryjnych konstrukcji metalowych (Application of damage mechanics in the analysis of pre-failure states of metal structures), *Zeszyty Naukowe Politechniki Rzeszowskiej Budownictwo i Inżynieria Środowiska* **59 (3/12/II)**,177-184.
20. Kossakowski, P 2012. Simulation of ductile fracture of S235JR steel using computational cells with microstructurally based length scales. *Journal of Theoretical and Applied Mechanics* **50, 2**, 589-607.
21. Kossakowski, P and Trąmpczyński, W 2012. Microvoids evolution in S235JR steel subjected to multi-axial stress state. *Engng. Trans*. **60**, **4**, 287–314.
22. Kossakowski, P 2015. Microstructural failure criteria for S235JR steel subjected to spatial stress states. *Archives of Civil and Mechanical Engineering* **15**, 195–205.
23. Kossakowski, P 2016. The influence of microstructural defects on the stress state of S235JR steel under plastic deformation. *Solid State Phenomena* **250**, 69–76.
24. Kossakowski, P 2017. Experimental determination of the void volume fraction for S235JR steel at failure in the range of high-stress triaxialities. *Arch. Metall. Mater*. **62, 1**, 167-172.
25. Kossakowski P, Wciślik W 2018. Numerical simulation of material damage for structural steels S235JR and S355J2G3, *Advances in Computational Design* **3, 2**,133-146.
26. Kossakowski, P 2018. Analysis of the void volume fraction for S235JR steel at failure for low initial stress triaxiality, *Archives of Civil Engineering* **64**, 101-115.
27. Kulak, GL and Wu, EY 1997. Shear lag in bolted angle tension members. *Journal of Structural Engineering* **123**, 1144-1152.

28. Može, P and Beg, D 2010. High strength steel tension splices with one or two bolts. *Journal of Constructional Steel Research* **66**, 1000-1010.
29. Munter, HLN and Bouwman, LP 1981. *Report: 6-81-21: Angles connected by bolts in one leg, Comparison to French, Eurocode 3, and Dutch formulae with the results of French and Dutch tests*, Stevin Laboratory, Department of Civil Engineering, Delft University of Technology.
30. PN-90/B-03200 Konstrukcje stalowe. Obliczenia statyczne i projektowanie, 1995.
31. Salih, EL, Gardner, L and Netherco,t DA 2010. Numerical investigation of net section failure in stainless steel bolted connections. *Journal of Constructional Steel Research* **66**, 1455-1466.
32. Sedlacek, G, Ungermann, D and Weynand, K 1988. *Evaluation of test results on bolted connections in order to obtain strength functions and suitable model factors – Part C: Test data, Eurocode No3 – Part 1- background documentation.* Brussels, Commission of the European Communities.
33. Sedlacek, G et al. 2008. *Commentary and worked examples to EN 1993-1-10 "Material toughness and through thickness properties" and other toughness oriented rules in EN 1993*, JRC Scientific and Technical Reports.
34. Snijder, HH, Ungermann, D, Stark, JWB, Sedlacek, G, Bijlaard, FSK and Hemmert-Halswick, A 1988. *Evaluation of test results on bolted connections in order to obtain strength functions and suitable model factors – Part A: Results, Eurocode No3 – Part 1- background documentation.* Brussels, Commission of the European Communities.
35. Snijder, HH, Ungermann, D, Stark, JWB, Sedlacek, G, Bijlaard, FSK and Hemmert-Halswick, A 1988. *Evaluation of test results on bolted connections in order to obtain strength functions and suitable model factors – Part B: Evaluations, Eurocode No3 – Part 1- background documentation.* Brussels, Commission of the European Communities.
36. Tvergaard, V 1981. Influence of voids on shear band instabilities under plane strain condition. *International Journal of Fracture* **17, 4,** 389-407.
37. Tvergaard, V and Needleman, A 1984. Analysis of the cup-cone fracture in a round tensile bar. *Acta Metallurgica* **32, 1**, 157-169.
38. Qian, XD, Choo, YS, Liew, JYR and Wardenier, J 2005. Simulation of ductile fracture of circular hollow section joints using the Gurson Model. *Journal of Structural Engineering* **131(5)**, 768-780.
39. Xu, Y and Qian, Ch 2013. Application of Gurson–Tvergaard–Needleman constitutive model to the tensile behaviour of reinforcing bars with corrosion pits. *PLOS ONE* **8, No. 1,** 1-7.

Editor received the manuscript: 08.12.2019